Boundary-Layer Meteorol (2013) 147:443–468
DOI 10.1007/s10546-012-9795-5

ARTICLE

# The Phoenix Evening Transition Flow Experiment (TRANSFLEX)

**Harindra J. S. Fernando · Brett Verhoef · Silvana Di Sabatino · Laura S. Leo · Seoyeon Park**

Received: 20 March 2011 / Accepted: 12 December 2012 / Published online: 6 January 2013


**Abstract** Motivated by air quality and numerical modelling applications as well as recent theoretical advancements in the topic, a field experiment, dubbed transition flow experiment, was conducted in Phoenix, Arizona to study the evening transition in complex terrain (shift of winds from upslope to downslope). Two scenarios were considered: (i) the flow reversal due to a change of buoyancy of a cooled slab of air near the ground, and (ii) the formation of a transition front. A suite of in-situ flow, turbulence and particulate matter (PM) concentration sensors, vertically profiling tethered balloons and remote sensors were deployed, and a mesoscale numerical model provided guidance for interpreting observations. The results were consistent with the front formation mechanism, where it was also found that enhanced turbulence associated with the front increases the local PM concentration. During the transition period the flow adjustment was complex, involving the arrival of multiple fronts from different slopes, directional shear between fronts and episodic turbulent mixing events. The upward momentum diffusion from the incipient downslope flow was small because of stable stratification near the ground, and full establishment of downslope flow occurred over several hours following sunset. Episodic frontal events pose challenges to the modelling of

H. J. S. Fernando · S. Di Sabatino · L. S. Leo
Environmental Fluid Dynamics Laboratories, Department of Civil & Environmental Engineering and Earth Sciences, University of Notre Dame, Notre Dame, South Bend, IN 46556, USA
e-mail: Harindra.J.Fernando.10@nd.edu

L. S. Leo
e-mail: LauraSandra.Leo.13@nd.edu

S. Di Sabatino (✉)
Laboratorio di Micrometeorologia, Dipartimento DiSTeBA, Universita' del Salento, 73100 Lecce, Italy
e-mail: silvana.disabatino@unisalento.it

B. Verhoef · S. Park
Center for Environmental Fluid Dynamics, Department of Mechanical and Aerospace Engineering, Arizona State University, Tempe, AZ 85287-9809, USA
e-mail: brettverhoef@hotmail.com

S. Park
e-mail: ksunp@kepco-enc.com

the evening transition in complex terrain, requiring conditional parametrizations for subgrid scales. The observed increase of PM concentration during the evening transition has significant implications for the regulatory enforcement of PM standards for the area.

**Keywords** Complex terrain · Evening transition mechanism · Thermal circulation · Transition front · Turbulent mixing

## 1 Introduction

Most urban areas have developed in complex landscapes, spurred by their association with water resources, and thus atmospheric flow in complex terrain is intertwined with urban meteorological and air quality studies (Fernando et al. 2010). In the absence of synoptic flow, small-scale flow in complex terrain is dominated by thermal circulations, characterized by upslope (anabatic) and up-valley winds during the day and downslope (katabatic) and down-valley winds at night. Recent comprehensive reviews on this topic can be found in Whiteman (1990, 2000), Fernando (2010), and Zardi and Whiteman (2012). The literature on katabatic flows is extensive (Doran et al. 2002), on anabatic flows is substantial (Hunt et al. 2003; Princevac and Fernando 2007), but relatively few studies exist on the transition between the two types of flows (e.g., Nadeau et al. 2012). The morning transition from downslope to upslope flows has been addressed in a number of studies (Whiteman 1982; Whiteman and McKee 1982; Princevac and Fernando 2008), but the evening transition remains the least studied of all (Monti et al. 2002; Fernando and Weil 2010). Yet, as pointed out by Seinfeld and Pandis (1998), both transitions occur during typical traffic rush hours with highest pollutant emissions. Existing mesoscale numerical models fail to predict transition periods accurately (Lee et al. 2007), which has been a bane for predicting air pollution under peak emission conditions. Transition periods are replete with small space-time scale phenomena, for example, non-equilibrium (decaying) turbulence, flow instabilities and gravity currents. Their inclusion as subgrid phenomena is imperative if the transition predictions by mesoscale models are to be improved.

This paper presents the results of a field experiment called TRANSition FLow EXperiment (TRANSFLEX) conducted in Phoenix, AZ, with the aim of understanding evening transition mechanisms in complex terrain and the effects of attendant phenomena on local air quality. The experiment was, in part, supported by the Arizona Department of Environmental Quality (ADEQ) to investigate specifically the role of the evening transition on the episodic increase of particulate matter (PM) concentration observed in south-west Phoenix. Of special interest was $PM_{10}$, the PM of aerodynamic diameter 10 $\mu$m or less, which is a regulated criteria pollutant contributed by the entrainment of crustal material by wind-induced turbulence (US EPA 1996; Arimoto et al. 2005; Choi et al. 2006). This is in contrast to $PM_{2.5}$, another regulated PM variety, attributed mainly to combustion sources such as motor vehicles and power plants. One of the sites of TRANSFLEX, the Phoenix (PHX) site, consistently exceeded the $PM_{10}$ standards (50 $\mu$g m$^{-3}$, yearly average), which has predicated the entire Phoenix area of attaining the National Ambient Air Quality Standards (NAAQS). As well, the experiment was intended to elucidate physical mechanisms underlying the evening transition in complex terrain, which is the focus of this paper. Following the Introduction, plausible physical mechanisms of the evening transition are discussed in Sect. 2, followed by the experimental design in Sect. 3. An outline of mesoscale model simulation results is given in Sect. 4 to aid interpretation of observations, which are presented in Sects. 5 and 6. Conclusions are given in Sect. 7.

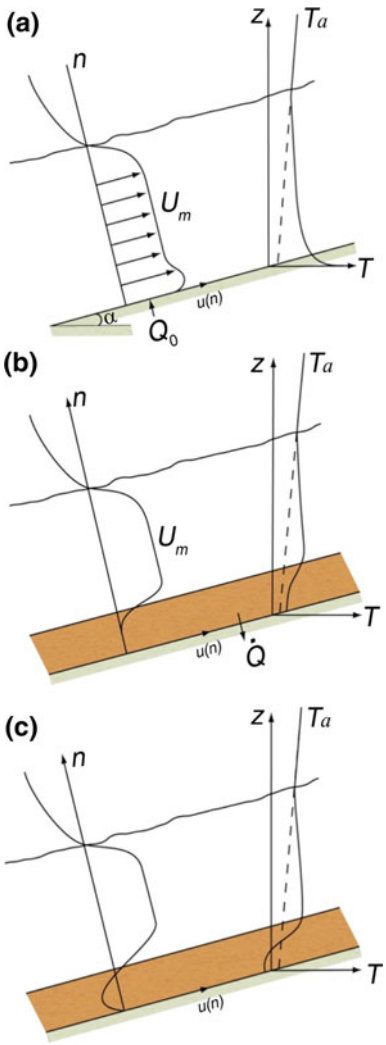


**Fig. 1** A schematic of the evening transition via a sliding slab of negatively buoyant fluid generated by radiative cooling near the ground. **a** Upslope flow. The *dashed line* is an extrapolation of outer temperature profile $T_a$ to illustrate the difference. **b** Stagnation due to an increase in the negative buoyancy to a critical value. The *shaded region* illustrates the cooled layer near the ground just before transition. **c** Downslope flow initiation

Although not discussed herein, a pattern recognition technique was developed to identify evening fronts using a network of meteorological stations operated by local agencies in Phoenix as well as using sensors at two TRANSFLEX sites. This system performed reasonably well, thus demonstrating the efficacy of cyber-infrastructure for future atmospheric research applications; further details are given in Yagnik et al. (2011).

## 2 Evening Transition Mechanisms

Two plausible evening transition mechanisms are discussed below, noting that the exact mechanism active in a particular case may depend on background conditions.

Figure 1 shows an anabatic flow on a slope $\alpha$ driven by a positive buoyancy flux $Q_0$, where the slope-normal ($n$) velocity profile $u(n)$ and the ambient vertical ($z$) temperature profile

$T_a(z)$ are shown in Fig. 1a. The forcing is then reversed to impose a negative buoyancy flux, whence the fluid layer near the ground undergoes cooling, becomes dense and finally stagnates (Fig. 1b). Thereafter, for weaker outer-layer stratifications, the characteristic temperature jump $\Delta T$ (the outside temperature minus the averaged temperature of the cooled layer of thickness $h$) becomes

$$\frac{\mathrm{d}\,(g\beta\Delta T h)}{\mathrm{d}t} \approx \dot{Q}, \tag{1}$$

where $\beta$ is the thermal expansion coefficient, $g$ is the acceleration of gravity and $\dot{Q}$ is the magnitude of the cooling buoyancy flux. The layer thickness grows as (Turner 1973, Chap. 7)

$$\frac{\mathrm{d}h}{\mathrm{d}t} \approx \frac{k}{h}, \tag{2}$$

where $k$ is a characteristic thermal diffusivity. For the layer to become increasingly dense and undergo a transition to a downslope flow (thus overcoming warming due to the downward heat diffusion at the top) requires $\mathrm{d}\,(g\beta\Delta T)/\mathrm{d}t > 0$, and using (1) and (2),

$$\frac{\dot{Q}h}{g\beta\Delta T k} > 1. \tag{3}$$

For the initiation of katabatic flow, the downslope buoyancy force ($g\beta\Delta T \sin\alpha$) needs to exceed the frictional forces i.e. $\nu U_\mathrm{c}/h^2$, where $\nu$ is a characteristic viscosity and $U_\mathrm{c}$ is the initial downslope velocity, with $U_\mathrm{c} \sim k/h$ (Turner 1973, Chap. 7). This, together with (1)–(3), provide a criterion for the initiation of downslope flow as a sliding slab of fluid (Fig. 1c), viz.,

$$R = \frac{\dot{Q}h^4 \sin\alpha}{\nu k^2} \gg 1, \tag{4}$$

or $R > R_\mathrm{c}$, $R_\mathrm{c}$ being a (modified) critical Rayleigh number to be determined through formal analysis. In this case, the flow stagnation and katabatic layer formation are associated with a transition from turbulent convection to a stably stratified atmospheric state that supports only a small turbulent heat flux.

An alternative model developed by Hunt et al. (2003) predicts a markedly different scenario. They considered an upslope flow on a simple slope subjected to spatially uniform cooling, realized by decreasing the temperature difference between the incline and ambient air. The model predicts the formation of a stagnation front (Fig. 2) around which existing upslope flow travels due to its inertia. The initial downslope motion of this transition front undercuts the upslope flow ahead and lifts the warmer fluid layers above the slightly cooled layer, in much the same way as a "paint stripper." The colder fluid behind the front is also lifted simultaneously by rising adjacent flow, and overturns as a result of convective instabilities. Stripped and rising fluid ahead of the front is entrained into the overturning region of turbulence and mixing. Highly jagged temperature structure of the mixing region is shown in Fig. 2 (left inset), and in an average sense the temperature is uniform therein. Behind the mixing region is the incipient katabatic flow, wherein a fall in temperature and damped turbulent intensities are expected. Continued cooling causes the front and trailing denser fluid to travel down the slope, establishing the katabatic flow.

Enhanced turbulence behind the front arguably is a mechanism of intense dust entrainment, especially $PM_{10}$, which remains airborne until the decay of turbulence (i.e. a few tens of minutes (Fernando 2010)). Hunt et al. (2003) demonstrated this front formation in the

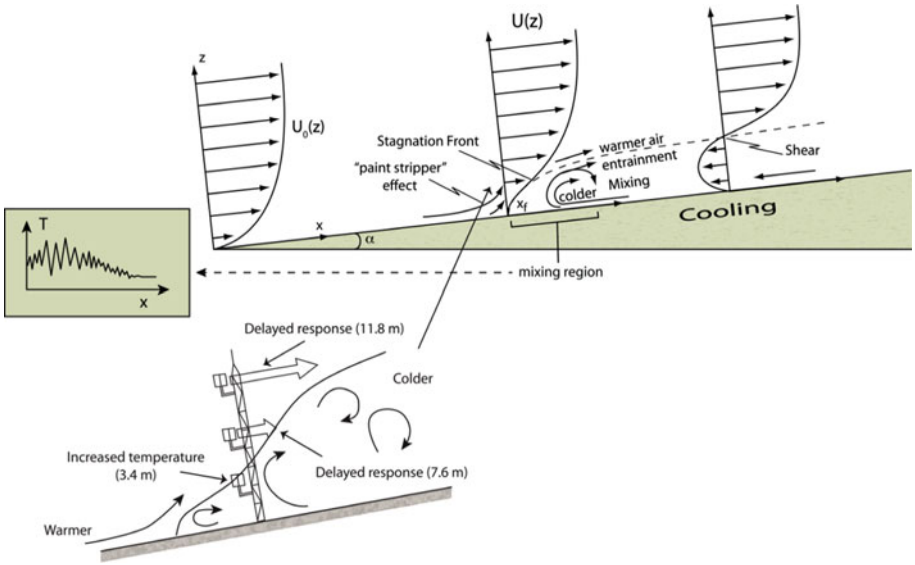


**Fig. 2** A schematic showing front formation associated with the evening transition on a slope of inclination $\alpha$. *Insets* Below the figure—delayed transition observed at upper levels; left of the figure—temperature structure of mixing region behind the front

laboratory by generating an upslope flow via heating a slope and then by gradually cooling it. Not all of their experiments produced a front, pointing to the possibility of other mechanisms. Infra-red thermal imaging in the Phoenix area has adumbrated the possibility of fronts arriving from nearby mountains (Fernando et al. 2010), but TRANSFLEX was intended to study them in detail.

## 3 Experimental Set-up and Selection of Design Days

TRANSFLEX was conducted between 7 and 17 January 2006 to observe the evening transition as it advances from the eastern slopes of Phoenix to the central city area (Fig. 3). The valley represents the Salt River basin that originates in the approximately 2,200 m tall mountains to the north-east, with a river bed running east to west. As part of the Colorado Plateau, these mountains bound the greater Phoenix area to the north and east. A steep drop results in Phoenix having an elevation of approximately 320 m. The smaller Sierra Estrella Mountains of the South Mountain Preserve demarcate the valley from the south. Because of the preponderance of sloping terrain to the east and north-east, the smaller mountains are generally considered unimportant for local meteorology but, as will be shown later, this was found not to be the case. Of interest were the characteristic changes in the flow, turbulence and PM during the evening transition, particularly in the context of concepts described in Sect. 2. To achieve these objectives, two measurement sites were selected by considering a mix of scientific requirements and logistical constraints, and the sites were instrumented with fast-response point and remote sensors.

The upslope location was at the Mountain View High School (MVHS) site in Mesa, AZ (33°26′14″N, 111°43′59″E; elevation 392 m above mean sea level, m.s.l.) as shown in Fig. 3a. It was in an agricultural area with scattered 1–2 storey homes nearby that offered a

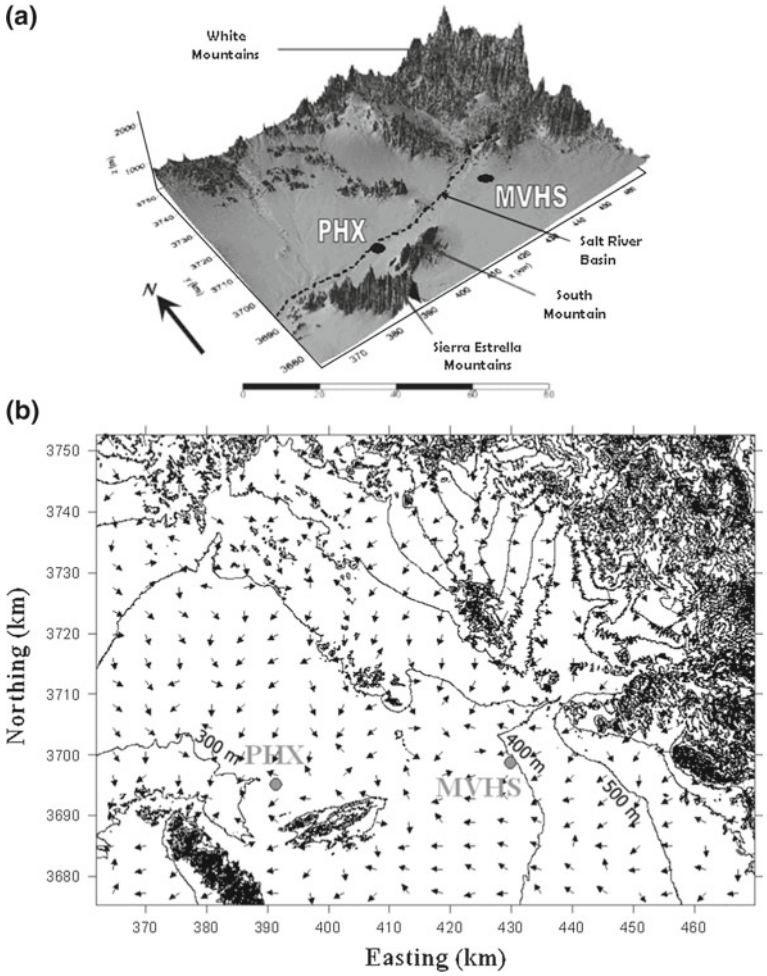


**Fig. 3** Phoenix valley with the two measurement sites indicated. Axes are in UTM (Universal Transverse Mercator) coordinates, zone 12. **a** Three-dimensional representation with the *dashed line* showing the Salt River basin; **b** 100-m elevation contours with the *arrows* indicating main drainage directions based on local slopes

fetch of ≈200–300 m in the upslope and downslope flow directions. The slope at the MVHS site is $\alpha = 0.00586$ rad (0.336°), the local drainage direction being 059° (north/north-easterly). Figure 3b shows elevation contours and local gradients. The instrumentation at the MVHS site included a mini sodar (AeroVironment), a tethered balloon carrying two tethersondes (AIR, TS-5A-SP; FAA restricted the maximum flight height to 50 m), a particulate matter analyzer (TSI, DustTrak) and a 12-m flux tower. Fitted to the tower were three ultrasonic anemometers at 3.4 m (Campbell Scientific, CSAT3), 7.6 and 11.8 m (RM Young, 81000) above the ground level (a.g.l.), a krypton hygrometer (Campbell Scientific, KH20) and a fine-wire thermocouple (Campbell Scientific, FW05) at 3.4 m, a net radiometer (Kipp & Zonen, CNR1) at 12 m, and an infrared thermometer (Everest, 4000-4ZL) to measure the soil surface temperature. A soil heat-flux plate (Hukseflux, HFP01SC-L) and four soil thermistors (Campbell Scientific, 107-L) were positioned beneath the soil at 0.065, 0.05, 0.04, 0.03 and 0.02 m, respectively.

The second measurement site (PHX) was at south Phoenix (33°24′22″N, 112°08′40″E; elevation 314 m above m.s.l.). The local slope of the site is $\alpha = 0.00231$ rad (0.132°) with 127° (east/south-easterly) drainage direction. The nearby topographic features included Mount Suppoa of the Sierra Estrella Mountains (820 m) to the south-west, South Mountain preserve to the south/south-east and the gradual (Salt River) valley slope shown in Fig. 3b. The instrumentation included two ultrasonic anemometers (RM Young, 81000), one on a tower at 10 m and the other on a tripod at 3 m a.g.l., a tethered balloon suspended with four tethersondes (Väisälä, TTS111) and a particulate matter analyzer (TSI, DustTrak), and a sodar/RASS (Scintec, MFAS). This site also had a suite of standard meteorological instruments operated by the Maricopa County Air Quality division, based on which 1-h averaged wind speed, wind direction and temperature at 10 m were available.

During 7–10 January, the balloons at both sites were in the *profiling mode*, ascending/descending between 2 and 45 m at a rate 0.2 m s$^{-1}$. During 11–17 January, the balloons were operated in the *tower mode*, where they were raised to 45 m and held throughout the evening. At the MVHS site the tethersondes were suspended on the line at 40 and 10 m a.g.l. and at the PHX site at heights 32, 21, 7, and 5 m a.g.l. Although the profiling mode yielded improved vertical resolution (≈0.2 m), its temporal resolution is the same as the time for the balloon to ascend from the ground to its maximum height (≈3 min). Given the large temporal gradients in properties during the evening transition (Pardyjak et al. 2009; Nadeau et al. 2012), this resolution was insufficient and hence the tower mode was necessary to capture the evening transition. The measurement uncertainties, sunset times, as well as the instrument details, are further described in Verhoef (2006).

To facilitate discussions to follow, the diurnal cycles of meteorological variables at the MVHS site are shown in Fig. 4 for a seven-day period. The sunrise and sunset times are indicated, and standard nomenclature is used (0° = northerly and 90° = easterly; $+u$ component = westerly and $+v$ component = southerly; $w$ being the vertical flow velocity component, positive upward). Note the clear diurnal variation, except on the days with any synoptic influence (e.g., the evening of 9 January to the early morning of 11 January). In the morning, the average (katabatic) wind is easterly/north-easterly, which changes to a westerly/north-westerly anabatic flow around midday. During the evening transition the wind changes to a easterly/north-easterly, after transient oscillations. The morning transition at the MVHS site almost always lagged sunrise by several hours whereas the evening transition followed sunset, with a delay of at most 30 min. The former represents the dissolution of the wintertime stable boundary layer. On days of significant synoptic flow, the transition was ill-defined, with the influence of the large-scale flow penetrating to ground level (≈4 m s$^{-1}$). For detailed analysis of the evening transition, days with little synoptic influence were selected based on National Weather Service radiosonde records from Tucson and Flagstaff, AZ as well as in-situ near-surface winds. January 7–8 and 12–14 had ground level wind speeds $<2.5$ m s$^{-1}$ and well-developed slope flows, indicating weak synoptic influence. Since the 24-h period of 12 January is representative of low-synoptic forcing conditions, it was selected as the design day for analysis. The bulk flow features of January 7–8 and 13–14 were similar to this design period.

## 4 Simulations of Flow Patterns Using MM5-URBAN

To aid the interpretation of observational data, especially those at the most complex site PHX, an urbanized (non-hydrostatic) version of the mesoscale model MM5 (MM5/Urbanized) was used for Phoenix following TRANSFLEX. The model is a variant of the Dupont et al. (2004)

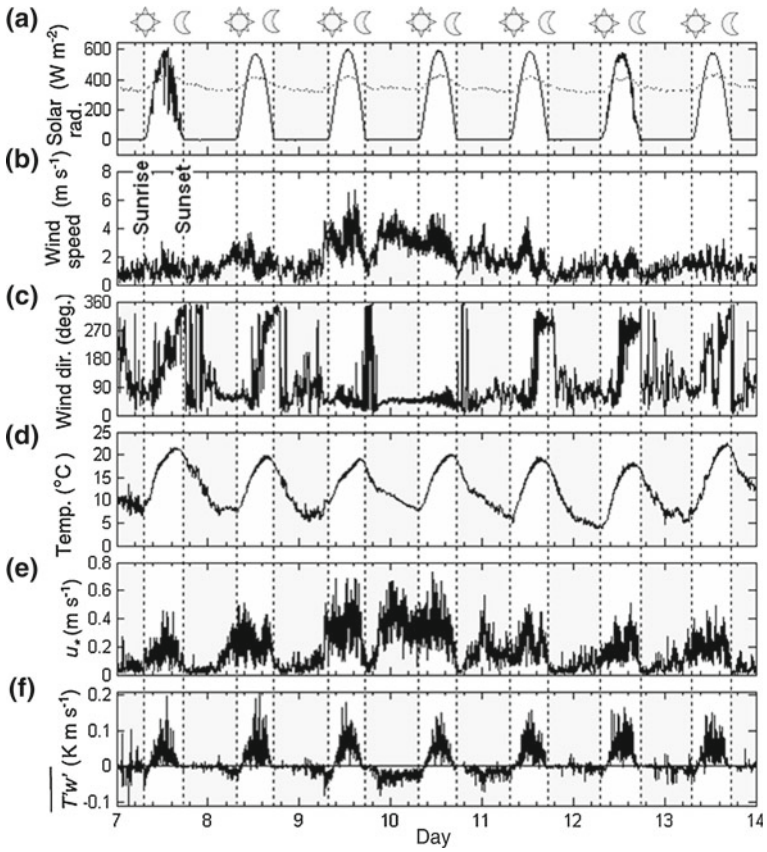


**Fig. 4** Time series from 7-13 January 2006 showing typical diurnal behaviour: **a** incoming shortwave radiation (*solid line*) and outgoing longwave radiation (*dotted line*), **b** horizontal wind speed, **c** wind direction, **d** temperature, **e** friction velocity, and **f** sensible heat flux. Measurements are 2-min averages from the MVHS site, 11.8 m

model, which couples the Penn State/NCAR Mesoscale Model MM5 with an urban canopy parametrization (UCP) scheme. The details of the model and its performance are given in Dupont et al. (2004) and its application to the Phoenix airshed, including model set-up, modifications and performance evaluation, is described in Park and Fernando (2006). For our purpose, the model was operated in a two-way nested configuration for several periods of January 2006, including 0000 LST (Local Standard Time) 12 January–0000 LST 14 January, with a spin-up period of 12 h. The five nested MM5 computational domains used include 81, 27, 9, 3, and 1-km horizontal grid resolution centered at metropolitan Phoenix. The first four domains were run with 36 vertical layers, with 17 layers in the planetary boundary layer, the lowest layer being at 10-m height. The 1-km domain had 181 $\times$ 85 grid points covering the Phoenix metropolitan area with 36 vertical layers, including 16 layers in the lowest 1 km, the lowest height being 4 m. The latter did not include a four-dimensional data assimilation procedure in order to minimize the influence of data ingestion. The 1-km domain used initial and boundary conditions that are interpolated from simulations with a 3-km domain.

A 1.5-order closure for turbulent kinetic energy (TKE) based on the Gayno–Seaman planetary boundary-layer (GSPBL) scheme (e.g., Shafran et al. 2000), a modified soil model (Dupont et al. 2004), a rapid radiative transfer model for longwave radiation, the Dudhia shortwave radiation scheme (Dudhia 1989), mixed-phase microphysics, explicit convection and the Noah land surface model (LSM) (e.g. Chen and Dudhia 2001) were used for MM5/Urbanized. The soil layers consisted of three layers with 0.01, 0.04 and 0.10 m deep layers from the surface, allowing calculations of evaporation from bare soil; this was required to assess heat fluxes at each level inside the canopy. Simulation results were later evaluated using TRANSFLEX data as well as observations gathered from 15 surface air monitoring stations operated by the Maricopa Associations of Government (MAG) in Arizona (to be presented in a later publication).

Figure 5a–c show vector plots of three representative flow patterns at 10-m height simulated for 12 January 2006. Comparisons of predicted wind direction (circles) with observations (lines) for selected times are shown in Figs. 6 and 7. Notwithstanding usual model errors and parametrization difficulties, a good qualitative (and sometimes quantitative) agreement could be seen between the predicted and observed wind directions at the MVHS and PHX sites. For example, for the MVHS site (Fig. 6), at 0800 LST, downslope directed winds are evident in both predictions (south-easterly) and observations (north-easterly/easterly). The morning transition is at 1200 LST in simulations and observations, and at 1400 LST the wind directions were 270° for both (Fig. 6). Prior to the evening transition, at 1700 LST, the model showed north-westerly/westerly flow (Fig. 5a), consistent with the measurements. The evening transition also is in general agreement with the model simulations and data (Figs. 5b, c, 6). The north-easterly winds evident at the MVHS site at 2000 LST are in agreement with the predictions.

The flow at the PHX site is complex, being affected by the presence of smaller mountains to the south and to the south-west/east. The observed and modelled flow directions at 1400 LST (both south-westerly) and 1700 (north-westerly in the observation and westerly in the model) were in good agreement (Figs. 5a, 7). The agreement at 1800 (north-westerly/south-westerly) was fair. Close to 1900 LST, the data showed a rapid transition to southerly and then south-easterly flow, veering clockwise, indicating the arrival of the downslope flow; this appears to represent the combined effects of the South Mountain range and the Sierra Estrella mountains (Figs. 3a, 5b). At 2000 LST, the influence of mountains to the south is still evident, and the flow is south-easterly in both the model and the 3-m data (Figs. 5c, 7). Close to 1930 LST, the flow at 10-m height underwent a rapid change of direction, making it difficult to conduct model and data comparisons.

Although the model and observations had clear quantitative disparities, the general flow patterns in the model simulations were useful to identify transition scenarios. The model did not support the commonly held notion (and our experimental planning assumption) that high mountain ranges to the east and north-east would produce a dominant evening-transition front, first arriving at the MVHS site and then at the PHX site. The simulations produced a significant transition flow from smaller mountains to the south that arrived at the PHX site first, overshadowing the influence of the north-eastern mountains. In fact, there is a flow convergence zone between the two sites (Fig. 5b, c, solid line), precluding direct interaction of transition fronts passing through the MVHS and PHX sites. This convergence zone has also been noted by Lee et al. (2003) in relation to katabatic flows in the early morning. Therefore, it was decided to analyze and interpret TRANSFLEX observations at the two sites separately without referring to their progeny.

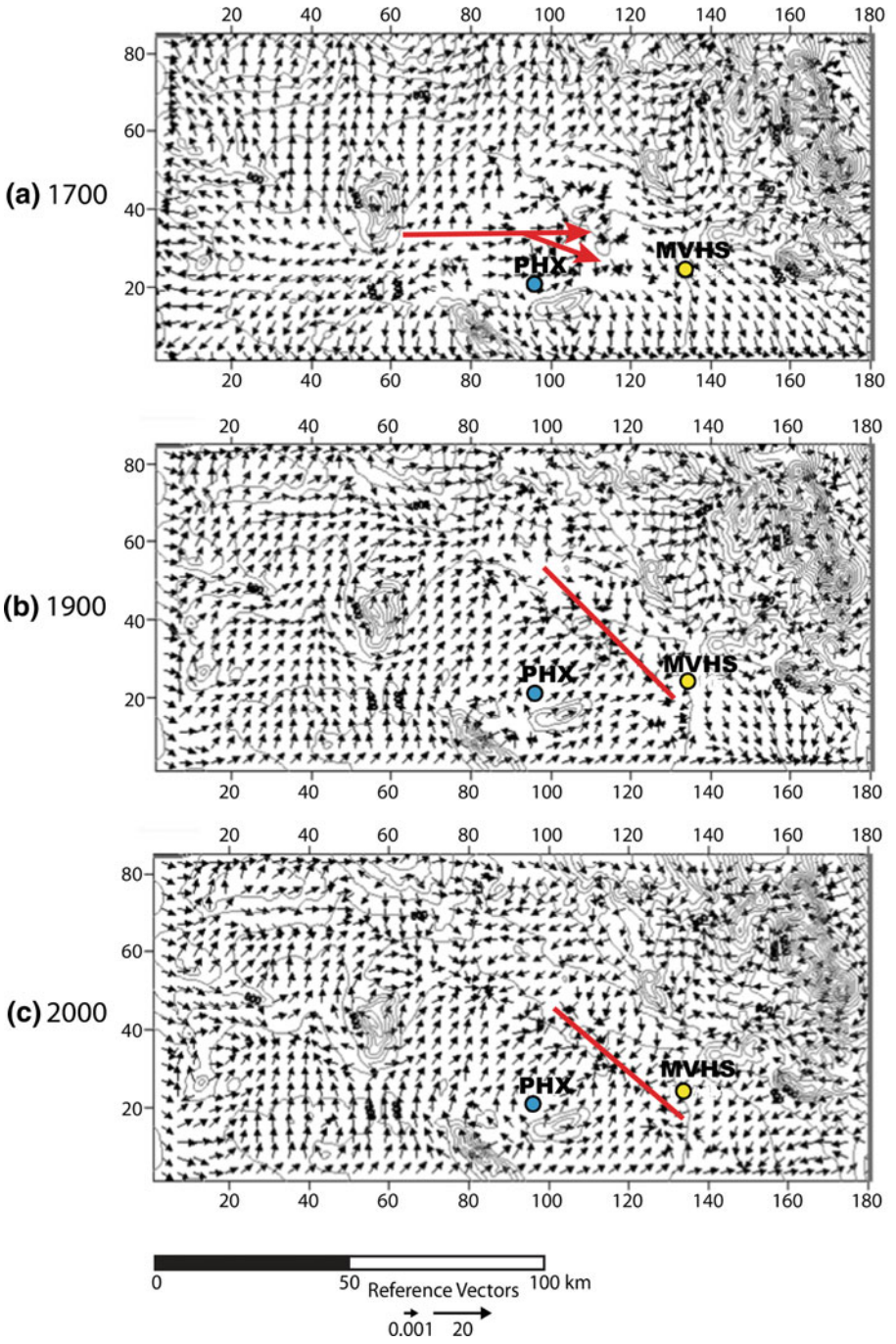


**Fig. 5** Flow patterns throughout the Phoenix valley at 10 m a.g.l. generated by MM5/urbanized model for 12 January 2006 at **a** 1700, **b** 1900, and **c** 2000 LST. *Circles* indicate the locations of the TRANSFLEX measurement sites. The general flow features (upslope flow in **a** and convergence in **b** and **c**) are indicated. The reference velocity vector in the bottom panel is in m $s^{-1}$

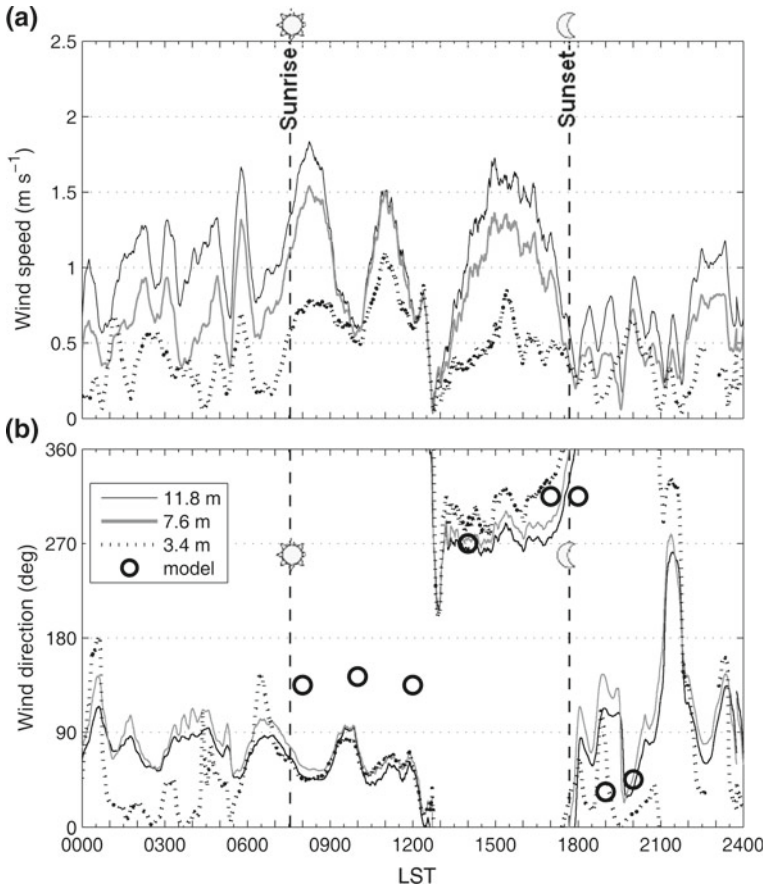


**Fig. 6** The 24-h time series of 30-min running averaged **a** total wind speed and **b** wind direction on 12 January 2006, MVHS. Sunrise (0733 LST) and sunset (1741 LST) times are shown. The simulated wind directions for selected hours are shown in *circles*. The transition is rapid and actually goes through north-west → north → east; cf. Figs. 9 and 10

## 5 General Observations

Wind speed and direction at the MVHS site are shown in Fig. 6, and corresponding changes at the PHX site are presented in Fig. 7. Some general inferences based on these observations can be drawn:

(i) On a typical non-synoptic day, the daytime sensible heat flux $\overline{w'T'}$ is ≈0.10 K m s$^{-1}$ (Fig. 4f), equivalent to a buoyancy flux of $g\beta\overline{w'T'} \approx 3.25 \times 10^{-3}$ m$^2$ s$^{-3}$, where $\beta = \theta_0^{-1}$, the reference potential temperature being $\theta_0$. With the daytime height of the convective boundary layer (CBL) $h_i \approx 700$m (estimates from RASS data—the height where temperature profiles show a well-defined inversion), the convective velocity becomes $w_* = \left(g\beta\overline{w'T'}h_i\right)^{1/3} \approx 1.3$ m s$^{-1}$, which is on the order of the upslope flow velocity recorded by sonic anemometers. According to Hunt et al. (2003), the upslope flow velocity is given by

$$U_m = \lambda_u \alpha^{1/3} w_*, \tag{5}$$

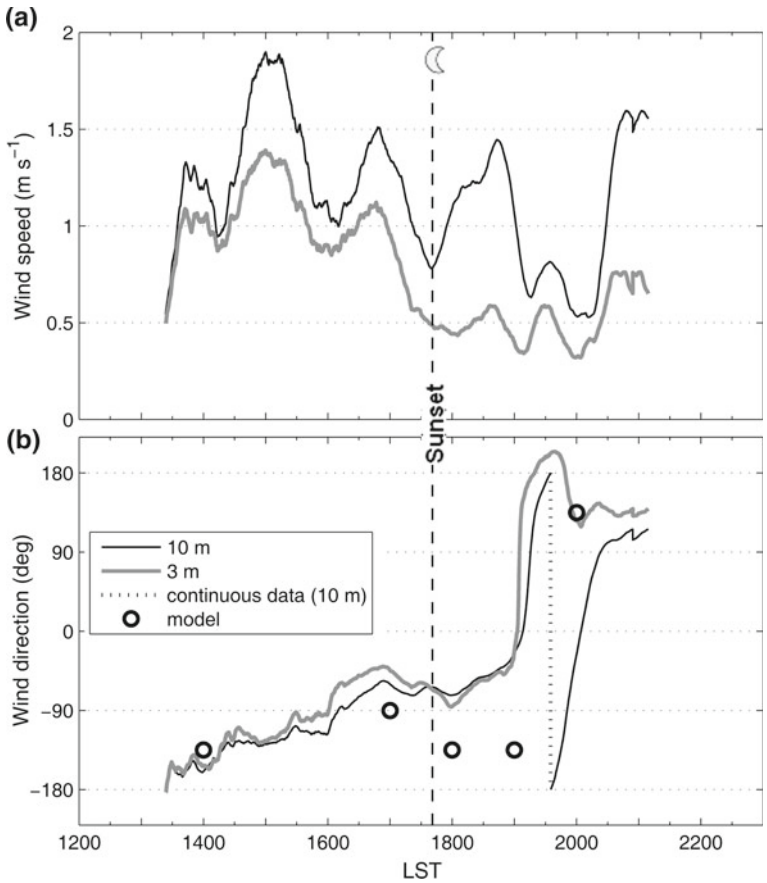


**Fig. 7** An 8-h time series of 30-min running averaged **a** total wind speed and **b** wind direction observed on 12 January 2006 at the PHX site. Sunset is at 1741 LST. The simulated wind directions for selected times (e.g. Fig. 5) are shown in *circles*

where $\alpha$ is the mountain slope, $\lambda_u = \ln(L_*/z_0)/\kappa$, $L_* = h_i(u_*/w_*)^3$ is the Obukhov length, $u_*$ is the friction velocity, $z_0$ is the aerodynamic roughness length and $\kappa \approx 0.41$ is the von Karman constant. With a characteristic observed value of $U_m \approx 1.5\,\mathrm{m\,s^{-1}}$ at 10 m for the MVHS site, it is possible to estimate $\lambda_u \approx 6.4$. Alternatively, a direct estimate for $\lambda_u = \ln(L_*/z_0)/\kappa \approx 4$ can also be made, based on $u_* \approx 0.2\,\mathrm{m\,s^{-2}}$ (Fig. 4e) and $z_0 \approx 0.5\,\mathrm{m}$. The latter estimate is close to that from the TRANSFLEX observations and estimates of Chan (2001), $\lambda_u \approx 6.6$, made on a smooth laboratory incline. The upslope flow velocity at the PHX site is also about $1.5\,\mathrm{m\,s^{-1}}$ (oscillating with a period of about 2 h), yielding $\lambda_u \approx 6.4$. The agreement between different cases is in part due to a weak (logarithmic) dependence of $\lambda_u$ on $L_*$ and $z_0$. A typical upslope flow velocity away from the ground (>20 m) provided by the MVHS sodar was ≈2–3 $\mathrm{m\,s^{-1}}$ (e.g. Fig. 8a).

(ii) Based on the "front formation" model of Hunt et al. (2003), Brazel et al. (2005) estimated the time for flow reversal since the initiation of cooling as

$$t_R \approx \frac{\pi \lambda_u^{1/2} \alpha^{-1/3}}{2} \left( \frac{\Delta t_0 w_*}{\Delta b_0} \right)^{1/2}, \tag{6}$$

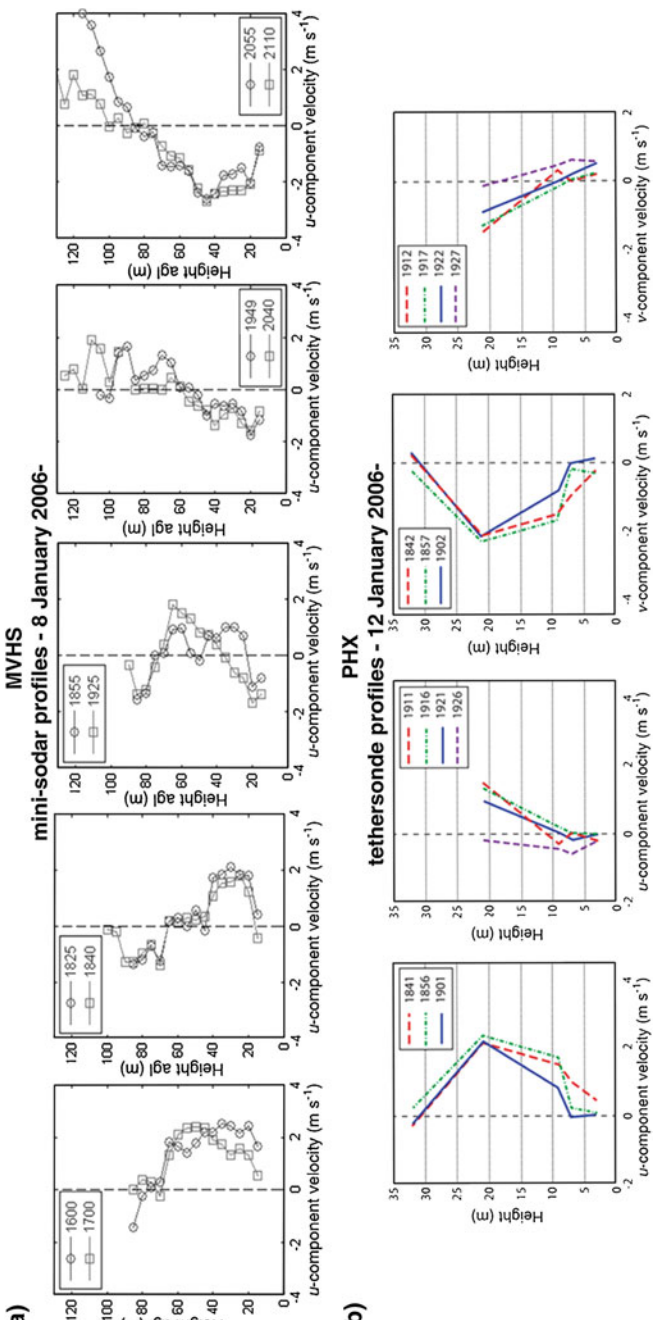


**Fig. 8** **a** The evolution of evening transition recorded by MVHS mini-sodar on 8 January 2006. Plotted are 5-min averaged $u$-component velocity profiles. The sunset was at 1737 LST; **b** Evening transition on 12 January 2006, PHX recorded by the tethered balloon with tethersondes at 32, 21, 9, and 7 m a.g.l. and an ultrasonic anemometer at 3 m a.g.l. Plotted are 5-min averaged $u$- (first and second panels) and $v$-components (third and fourth panels) velocity profiles. The sunset was at 1741 LST. The 32-m sonde malfunctioned for data in second and fourth panels

where $\Delta b_0$ is the initial buoyancy jump across the upslope flow layer and $\Delta t_0$ is the time scale of cooling. Conversely, according to the slab model in Sect. 2, the transition time can be estimated using (2) and (3) as

$$t_R \approx \frac{R_c^{1/2}}{2}\left(\frac{\nu}{\dot{Q}\sin\alpha}\right)^{1/2}, \tag{7}$$

indicating that for both scenarios the transition first occurs on steeper slopes. For the airshed considered, this corresponds to the eastern mountains, the influence of which is expected to propagate down the slopes, first arriving at the MVHS site and then at the PHX site; this has been the common belief of local air quality personnel (Fernando et al. 2001). While this scenario nominally appears to be the case, whereas on non-synoptic days the evening transition at the PHX site follows the MVHS site by 0.5–1.5 h, close inspection reveals that a front propagating from the eastern mountains cannot reach the PHX site so quickly, given the frontal propagation speed of $U_F \approx (g\beta\Delta T h)^{1/2} \approx 1\ \mathrm{m\ s^{-1}}$ based on MVHS observations ($\Delta T \approx 3$ K, $h \approx 10$ m) and the distance between the sites of 37 km. Another possibility would be an additional transition from westerly to easterly flow over the gently sloping valley (in addition to that over the eastern mountains), but neither the observations of Figs. 6 and 7 nor the mesoscale simulations of Fig. 5b, c support this notion. Both indicate arrival of the first katabatic front at the PHX site from the south/south-east. As such, evening transitions at the MVHS and PHX sites appear to be independent.

(iii) The flow reversal at greater heights takes place slowly following the near-surface (<10 m) reversal. As pointed out by Brazel et al. (2005), this may be due to the weak transport of momentum across (or weak Reynolds stresses within) the stable density interface that tops the katabatic flow. Mini-sodar profiles at the MVHS site shown in Fig. 8a for January 8 indicate that flow reversal at 20 m did not take place until 1840 LST although a transition at ground level (tower data) occurred at about 1750 LST (Verhoef 2006). Furthermore, the full establishment of (≈80 m thick) katabatic flow did not occur until 2055 LST. This delay of about 2 h from the first evidence of flow reversal at ground level is consistent with the estimates of Brazel et al. (2005). They argued that the downslope flow establishment at upper levels has a time delay of

$$T_d = 2\left(\frac{U_m}{\sigma}\right)\left(\frac{h}{\sigma}\right) = 2\lambda_u\alpha^{1/3}\left(\frac{w_*}{\sigma}\right)\left(\frac{h}{\sigma}\right), \tag{8}$$

where $\sigma$ is the root-mean-square (r.m.s.) velocity and $h$ is the original anabatic flow depth. With $\sigma \approx 0.5\ \mathrm{m\ s^{-1}}$, $w_* \approx 1.3\ \mathrm{m\ s^{-1}}$, $h \approx 700$ m, we obtain $T_d \approx 2.3$ h.

Tethersonde observations at the PHX site at 32, 21, 9 and 7 m heights for January 12, with the balloon in the tower mode, also show that the flow reversal at low levels started at around 1900 LST, but at 20-m height did not occur until 1926 LST, about 1.75 h after sunset and 30 min after the wind shift at low levels (Fig. 8b).

(iv) The MVHS site wind-speed records of Fig. 6 show nocturnal oscillations between 0000–0600 LST with a period of about 1 h. This is consistent with the along-slope oscillations of the katabatic flow predicted by Princevac et al. (2008), having a frequency of oscillations $\omega_N = N\sin\alpha$, $N$ being the background frequency. For this particular site $N = 0.25\ \mathrm{rad\ s^{-1}}$ (measurements at 3.4 and 11.8 m), $\alpha = 0.336°$, and hence $\omega_N = 1.5 \times 10^{-3}\ \mathrm{rad\ s^{-1}}$ and $T \approx 1.2$ h. During periods of weaker stratification (2000–2400 and 0600–1000 LST), the oscillation period was larger on the order of $T \approx 3$ h.

(v) Schumann's (1990) linearized analysis predicts upslope flow oscillations, also with a frequency $N\sin\alpha$. Based on the estimates of ambient $N$ (≈0.1 rad s$^{-1}$), the period of oscillations

**Table 1** Comparisons between two transition mechanisms

| | Slab flow (Fig. 1) | Front formation (Fig. 2) |
|---|---|---|
| Mean velocity | The upslope flow gradually weakens, stagnates and starts reversing. The reversal is uniform along the slope. The upslope flow at higher elevations may continue for some time | The flow stagnates at the front. Upslope flow reverses, undercutting and raising the flow down the slope like a "paint stripper." When the front arrives at a particular location, the flow momentarily stagnates and then reverses. The evening transition thus is a propagating phenomenon at lower elevations. Transition at intermediate heights happens a few minutes later than that at the ground level (Fig. 2, lower inset). Upslope flow at higher elevations may continue for some time |
| Temperature | Gradual reduction. No rapid jumps and strong fluctuations | First increases ("paint stripper") and then decreases. Strong fluctuations and mixing behind the front |
| r.m.s. fluctuations | Weak. Stable stratification inhibits mixing. Fluxes are small. Internal waves can be present | Strong r.m.s. fluctuations of temperature and velocities. Fluxes can be significant due to mixing, followed by suppression due to stable stratification |

becomes 3 h for the MVHS site and 7.5 h for the PHX site. While upslope flow oscillations were unidentifiable at the MVHS site (Fig. 6), oscillations were evident at the PHX site with a period ≈2 h (Fig. 7). As such, we surmise that Schumann's analysis is inapplicable for the case considered.

## 6 Detailed Observations on Flow Transition

In Sect. 2, two scenarios for evening transition were identified: the *slab flow* and *front formation*. The attributes of each mechanism are summarized in Table 1 for reference, and below we attempt to compare transition observations with each of these scenarios.

### 6.1 Evening Transition at the MVHS Site

Figure 9 shows (a) the wind velocity components at 11.8 m, and (b) air temperature, and (c) wind direction at 11.8 and 3.4 m based on raw data. Note the change in wind direction at 1749 LST at 3.4 m and 1753 LST at 11.8 m (Fig. 9c). Associated with the wind shift is a glaring flow stagnation (Fig. 9a) and an increase in temperature at the 3.4 m level (Fig. 9b), indicating the 'paint stripper' effect (Fig. 2). The negative fluctuation in temperature at 7.6 and 11.8 m indicate lifted cold air blobs, causing the heat flux to fluctuate and change sign. As the front passes at the upper levels (level 11.8 in Fig. 9b), air temperature at these levels gradually decrease as a result of the passage of colder air in the mixing layer behind the front. Although the initial temperature responses at higher and lower levels are different, soon they assume similar temperatures as the front evolves. These observations are in good

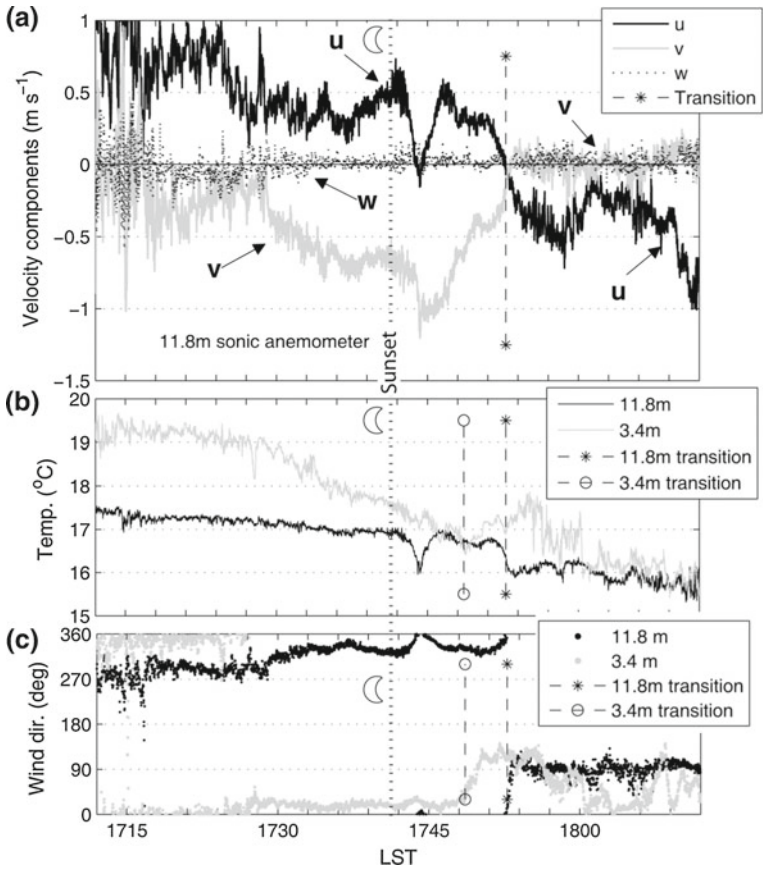


**Fig. 9** Raw data from 12 January 2006, MVHS site, showing time series plots of **a** velocity components at 11.8 m, **b** temperature at 11.8 and 3.4 m, and **c** wind direction at 11.8 and 3.4 m during evening transition. The sunset was at 1741 LST

agreement with the front formation scenario rather than the slab flow transition (Table 1). The difference in the time of arrival at the two levels is an indication of the sloping nature of the front (Fig. 2, lower inset). The typical slope (nose) angle of the front, based on Princevac (2003), is 15–20°.

To illustrate the intricacies of flow adjustments following transition, Fig. 10 shows a 3-h time series of temperature and wind direction for three different heights. For example, in Fig. 10c, the evening transition is clear at 1749 LST with the flow direction changing in succession from the lowest to the highest level of sonic anemometers (Fig. 10a, b), consistent with an inclined front. The temperature increase at the 3.4 m sonic is in agreement with the 'paint-stripper' effect. Figure 10d superimposes all three levels, to illustrate small-scale variability and the layered nature of the near-surface flow. The increase of r.m.s. fluctuations following the transition (Fig. 11a–d) also supports the front formation mechanism, where about 25–100 % increase in the r.m.s. velocities above the pre-transition values is noted. The r.m.s. temperature fluctuations at the lower levels increase by a factor of 3–4. Because of warmer air entrainment into the front and the descent of lifted colder air, the heat flux behind

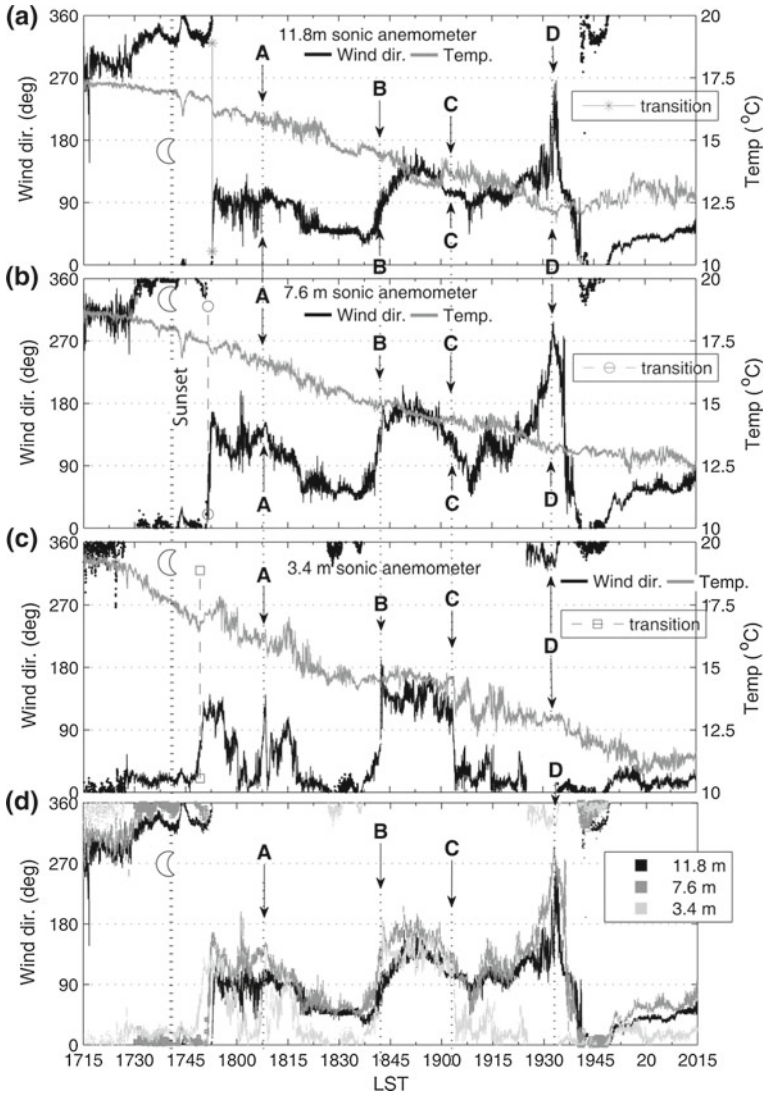


**Fig. 10** 3-h time series of wind direction and temperature for 12 January 2006 at the MVHS site from ultrasonic anemometers at **a** 11.8 m, **b** 7.6 m, **c** 3.4 m a.g.l. Superimposed on (**d**) are wind directions of all three anemometers. In (**a**)–(**c**), the arrival time of first evening transition front is shown. Also identified (A–D) are significant disturbances/events following the first front, which are also marked in Figs. 11 and 12. Measurement rate was 10 Hz; sunset was at 1741 LST

the front oscillates between negative and positive values (Fig. 11e–g). The elevated turbulent fluctuations last for tens of minutes.

As mentioned, the evening transition is followed by a series of flow adjustments, identified as A, B, C and D. For example, the flow perturbation A at 3.4 m is felt only mildly at the other two heights (Fig. 10), indicating a ground level intrusion that arrives from topographic features to the east/south-east, undercutting low-level air. This feature creates vertical *directional* shear between the layers (Fig. 10d), which lasts for ≈10 min. The computed 1-min averaged

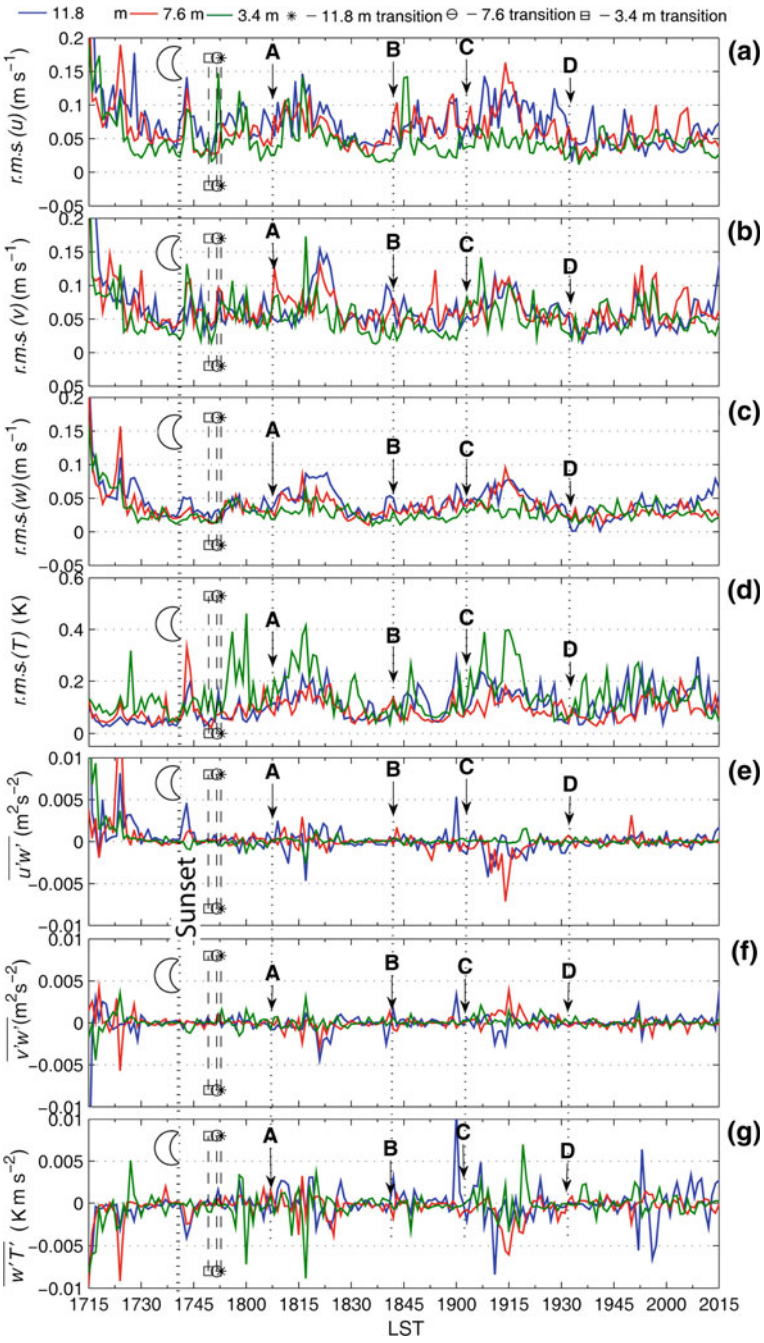


**Fig. 11** Same as in Fig. 10 but r.m.s. quantities for **a** $u$-component velocity, **b** $v$-component velocity, **c** $w$-component velocity, **d** temperature; and **e** $\overline{u'w'}$, **f** $\overline{v'w'}$, **g** $\overline{w'T'}$, where $T$ is the temperature. 1-min averages were used. The time of sunset (1741 LST) is identified

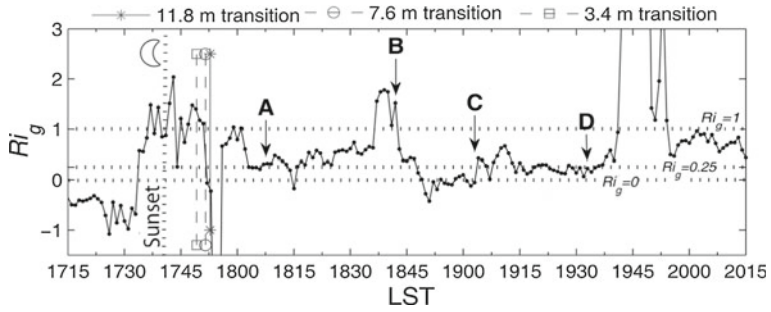


**Fig. 12** Same as in Fig. 11, but the time evolution of 1-min averaged gradient Richardson number $Ri_g$ is shown. The *dotted lines* correspond to $Ri_g = 0$, 0.25 and 1, corresponding to the thresholds of instabilities identified by Strang and Fernando (2001)

gradient Richardson number $Ri_g$ between 3.4 and 7.6 m (Fig. 12) decreases from $Ri_g \approx 1$ before the event to $Ri_g \approx 0.25$ during the event, where

$$Ri_g = \frac{N^2}{\left(\frac{\Delta u}{\Delta z}\right)^2 + \left(\frac{\Delta v}{\Delta z}\right)^2}, \tag{9}$$

$\Delta z$ is the vertical separation and $\Delta u$ and $\Delta v$, respectively, are corresponding $(u, v)$ velocity differentials. Note that the upstream influence causes $Ri_g$ to change before the arrival of front, which is a characteristic of intrusions into stratified fluids (De Silva and Fernando 1998). According to Strang and Fernando (2001), this decrease in $Ri_g$ facilitates significant mixing via Kelvin–Helmholtz (K–H) instabilities. Strang and Fernando (2001) identified $Ri_g \leq 0.25$ as a regime with significant mixing due to K–H instabilities, $0.25 \leq Ri_g \leq 1$ as where K–H and internal waves co-exist and resonate with each other, and $Ri_g > 1$ as where mixing becomes weak although sporadic Hölmböe instabilities may be present. The increase in r.m.s. fluctuations, Reynolds stresses and heat fluxes following perturbation A support this assertion (Fig. 11). Continued directional shear has helped to maintain $Ri_g \approx 0.25$ for a short period, including some overturning where $Ri_g < 0$, but an increase in $Ri_g$ thereafter produced turbulent decay.

A southerly pulse of air that affects all three levels and lasts for about 15 min appears at B, followed by a northerly pulse near the ground at C. The decrease in $Ri_g$ during perturbation B triggered overturning motions, which continued until C. Again the directional shear appeared between 3.4 m and the other two sonic anemometers following C, lasting for about 45 min, thus facilitating low $Ri_g$ and sustenance of turbulence (Fig. 11).

At 1933 LST, a westerly pulse of air intruded above the bottom layer (event D) while setting up a stronger stable stratification and low directional shear, leading to large $Ri_g$ during 1940–1950 LST. This led to low turbulent mixing and smaller heat fluxes (Fig. 11), but to higher r.m.s. temperature and velocity fluctuations, which are presumably due to internal waves triggered by the disturbance. At 1955 LST, $Ri_g$ decreases to 0.25 facilitating the generation of turbulence but $Ri_g$ increases thereafter rapidly, reducing K–H activities.

In general, once the transition takes place, the flow tends to be variable over a period of time, with strong vertical directional shear due to density currents arriving from different directions and with varying densities. The local gradient Richardson number $Ri_g$ appears to be a good parameter to describe the effects of such variability, especially in predicting the generation of turbulence and the existence of non-zero fluxes. Note that these events

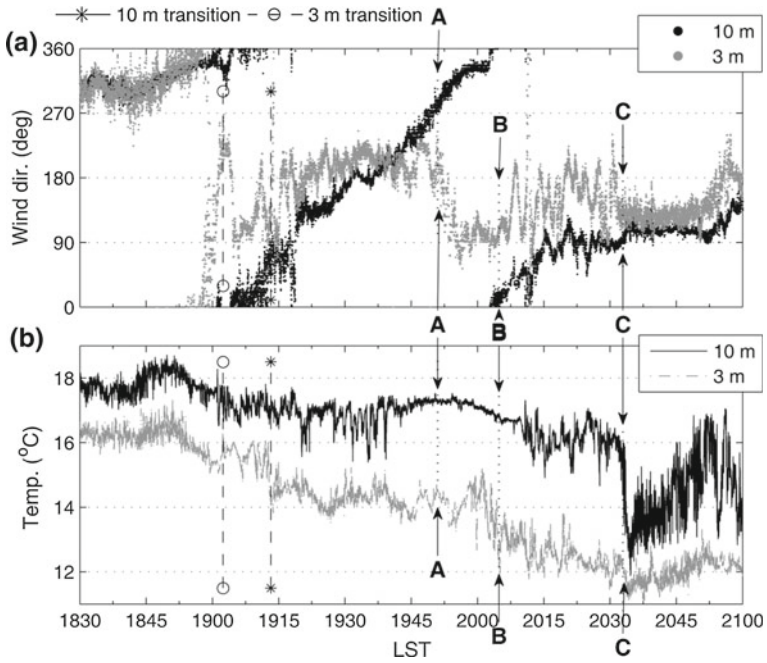


**Fig. 13** 2.5-h time series of **a** wind direction and **b** temperature on 12 January 2006, PHX site, for 10 m and 3 m a.g.l. Also identified are special events, A–C. These features are also identified in Fig. 14. Measurement rate was 10 Hz; sunset was at 1741 LST

occur over times scales of minutes, and hence differ from $Ri_g$ variability and turbulence generation in the stable boundary layer over complex terrain that take place over a period of hours. Pardyjak et al. (2002) identified the latter as a locally driven phenomenon whereas the processes described above are triggered by basin scale processes such as intrusions arriving from different slopes.

Because ground cooling starts about an hour or so before the sunset, the r.m.s. velocities show a decreasing trend before the transition, but such effects are less pronounced on temperature fluctuations since thermals continue to rise from the ground for sometime (Cole and Fernando 1998). A similar result has been reported by Caughey and Kaimal (1977) for the transition over flat terrain. In the period following the evening transition, the momentum and heat fluxes remain small as a result of stable stratification, except during special events such as perturbations A–D in Figs. 10, 11, and 12.

### 6.2 Evening Transition at the PHX Site

A 2.5-h data record surrounding the evening transition for wind direction and temperature at the PHX site is given in Fig. 13 for 12 January 2006, and the corresponding r.m.s. quantities are shown in Fig. 14. The momentum and heat flux variations, as well as the $Ri_g$ behaviour, were representative of the MVHS site and hence are not presented. Note the following general observations, subject to some specific isolated deviations due to natural variability.

- Before the transition, the flow is westerly/north-westerly with the stagnation (velocities $<0.5\,\mathrm{m\,s^{-1}}$) and flow switching occurring progressively at the 3-m sonic (around 1902 LST, Fig. 13), 10-m sonic (around 1913 LST, Fig. 13) and at the 20-m tethersonde (1926

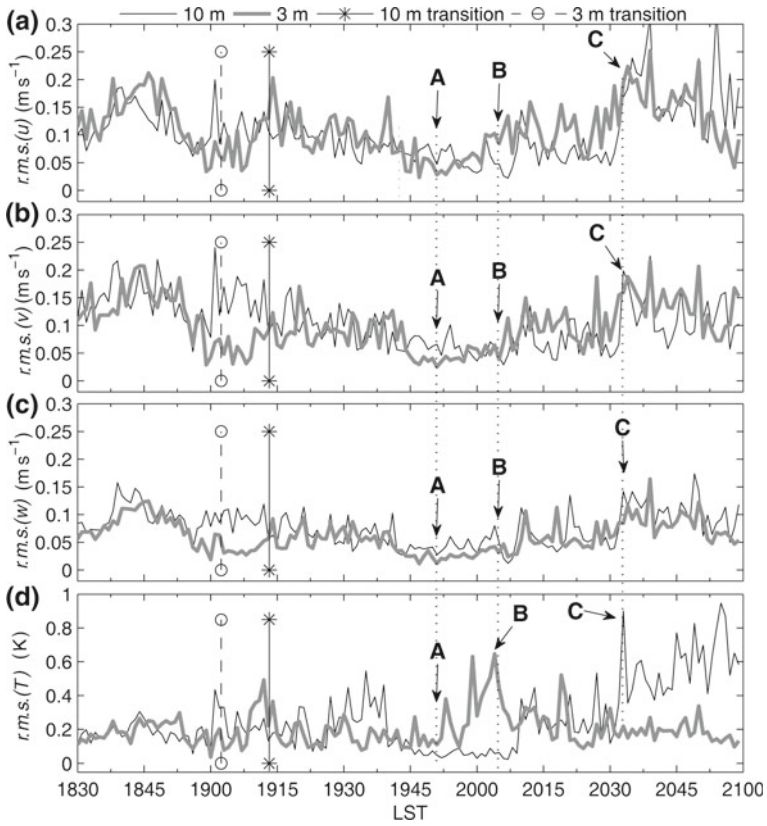


**Fig. 14** Same as in Fig. 13, but for r.m.s. quantities **a** $u$-component velocity, **b** $v$-component velocity, **c** $w$-component velocity, and **d** temperature. 1-min averages were used

LST, Fig. 8b). This consecutive flow reversal in the vertical, the slight warming recorded at the 3-m sonic, the enhanced r.m.s. fluctuations during flow reversal, indicate that the transition at the PHX site was associated with the arrival of a southerly/south-easterly flow. The MM5 model simulations track this transition flow to Mount Suppoa in the South Mountain area (Fig. 5b).

- Within the next 30-min the flow direction at both levels gradually changed to southerly (1939 LST, Fig. 13a). During the period 1913–1939 LST, the directional shear was large, but so is the stable stratification with a buoyancy jump of $\Delta b \approx g\beta\Delta T = 0.07\ \mathrm{m\ s^{-2}}$. The 1-min averaged $Ri_g$ based on 3- and 10-m sonic anemometers during this period was large, $Ri_g > 2$ (not shown). Therefore fluctuations seen during this period appear to be due to internal waves excited by the preceding transition.
- The wind direction at 10 m continued to change and became westerly at 1951 LST (event A) while at the 3-m level abruptly changing to easterly. The increase in temperature at 3 m while remaining constant at 10 m indicated the arrival of a southerly intrusion at low levels, producing an increase in temperature fluctuations at 3 m (Fig. 14d). The wind shear so generated reduced $Ri_g$ to $\approx$1, which is sufficiently low to cause K–H instabilities coexisting with internal waves.

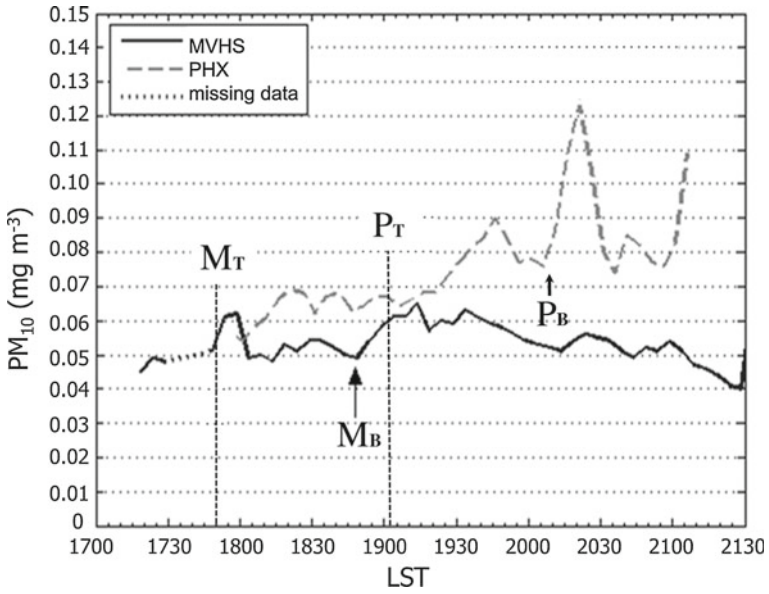


**Fig. 15** 5-Min averaged time series of $PM_{10}$ for both measurement sites on 12 January 2006. Identified are the onsets of $PM_{10}$ concentration spikes associated with increases of turbulence during events identified in the text. Measurement height was 2 m a.g.l., $P_T$ = transition time at the PHX site and $M_T$ = transition time at the MVHS site

- The event A was followed by event B (2005 LST) where the 3-m wind direction commenced to fluctuate rapidly, followed by the response at 10 m in terms of high r.m.s. fluctuations in both velocity components and temperature (Figs. 13, 14). The flow turned southerly, the 3-m temperature gradually fell by several K and fluctuations at 10-m level increased somewhat, indicating the undercutting of surface air by a colder air mass. At the onset of this event, $Ri_g$ fell to $\approx$0.25 and fluctuations in the lower layer were greatly enhanced due to turbulent mixing, but the stratification between the layers caused $Ri_g$ to rise ($>$3) subsequently.
- Strong mixing occurred at event C (2033 LST), where the air layer surrounding the 10-m sonic anemometer was vigorously mixed with cold air below, while turbulence levels at 3-m were low. The lower layer slowly became warmer following the event, indicating the gradual downward penetration of warmer air. The vertical mixing of momentum (as evidenced by the Reynolds stresses) erased the directional shear between 10 and 3 m (Fig. 14). Immediately after event C, the 1-min averaged $Ri_g$ decreased to, and was thereafter maintained at, 0.25, indicating sustained K–H instabilities and mixing. The penetration of mixing to the lower layer, however, still remained impeded as evident in the temperature data in Figs. 13 and 14.

### 6.3 Particulate Matter Episode

The $PM_{10}$ concentration measurements made using the DustTrak instruments are shown in Fig. 15, which characterize the mechanical (turbulent) entrainment of $PM_{10}$ from the ground during transition. At the MVHS site, where the first transition occurred at 1749 LST at a height of 3.4 m (and at 1753 LST at 11.8 m), there was a discernible increase in $PM_{10}$, coinciding

with the transition (indicated by $M_T$). Also, at $M_B$ (1845 LST), which was earlier identified as a southerly pulse B at ground level (Figs. 10–12), an increase of particle suspension could be observed. It is interesting to note that the intrusive feature D of Figs. 10 and 11 (1933 LST) is not associated with a significant spike in dust entrainment, given that it is disconnected from the dense layer near the ground by a stable density interface.

At the PHX site, following the transition at 1902 LST at 3-m height (and 1913 LST at 10 m), there was a tendency of particulate matter to increase as indicated by $P_T$. The particulate matter peaked in the proximity of the event A at 1951 LST, and again started rising at 2005 LST ($P_B$) and then peaked at around 2020 LST. This can be attributed to strong mixing events signified by high r.m.s. turbulence quantities and momentum fluxes (B in Figs. 13, 14). The concentration started rising again after 2033 LST, following event C, but the effects of strong mixing at C were less pronounced at the ground level as mixing occurred at about 10 m with little penetration to 3 m (Sect. 6.2). In general, the PHX site showed a high overall $PM_{10}$ concentration, given that the site and its proximity are unpaved, allowing direct contact between ground particulates and air aloft. On the other hand, the MVHS site is an area of covered land with short shrubs and vegetation, and thus the propensity for dust entrainment is lower.

In all, the particulate matter entrainment following the evening transition, as observed by the DustTrak instruments, coincided with increases in near-surface turbulence and wave disturbances, which appears to be determined by the arrival of fronts at ground level associated to the evening transition and following the mechanisms explained in the previous sections. More quantitatively, the dust events were related to the local $Ri_g$.

## 7 Conclusions

A field experimental study, dubbed TRANSFLEX, was conducted in the Phoenix airshed to investigate the mechanisms of evening transition in complex terrain and attendant local air quality issues. Two conceptual models: (i) sliding down of a dense slab of fluid upon exceeding a critical Rayleigh number, and (ii) front formation and its downslope propagation, guided the design of the experiment and interpretation. The former leads to simultaneous transition everywhere over the slope and monotonic evolution of meteorological variables. Conversely, the latter predicts stagnation of upslope flow at a particular location to form a front, down-the-slope of which the flow remains upslope while on the opposite side of the front the flow starts to drain (Hunt et al. 2003). Momentarily, the front starts to advance downslope with enhanced turbulence and mixing behind the front while raising isotherms ahead; thus an increase and then a decrease of temperature is noted at fixed sonic anemometers.

Two measurement sites were located along the valley: one at the Mountain View High School (MVHS) close to the eastern high mountains and the other in south Phoenix (PHX) where the particulate matter (PM) concentration is consistently high in the evening. This site violates the National Ambient Air Quality Standards (NAAQS) for $PM_{10}$. A summary of the study and results are given below, based on data taken on a representative, non-synoptic day: 12 January, 2006.

(i) At both the MVHS and PHX sites, the arrival of the first transition front was clearly evidenced by the momentary flow stagnation, the rapid change in wind direction, the transient increase of temperature at low levels (‘paint stripper’ effect) and enhanced turbulent fluctuations. These observations are consistent with the front formation model. After transient periods that involve arrival of fronts/intrusions from various other slopes, sustained downslope flow ensued.

(ii) The first front at the MVHS site arrived from the nearby mountains to the east, and at the PHX site from the mountains to the south/south-east. Front arrival times differ greatly: 1749 LST at the MVHS site and 1902 LST at the PHX site with sunset being at 1741 LST. Different directions of these flows led to complex flow circulations in the airshed. Subsequent fronts arriving as gravity currents sometimes overran the existing flow or undercut it, depending on their buoyancy. Such intrusive flows were responsible for the intermittent turbulence and mixing and, if close to the ground, for episodic dust entrainment events.

(iii) The MM5/urbanized model output aided the interpretation of measurements, and model predictions were in general agreement with observations, at least qualitatively. The simulations show that the transition front observed at the MVHS site can hardly reach the PHX site because of the existence of a convergence zone in between.

(iv) Local mixing events during and following the arrival of fronts played an important role in the flow evolution following transition. A local Richardson number criterion may prove useful in quantifying such events. Conditional parametrizations that can trigger mixing events within computational grids are recommended for mesoscale numerical models, as was attempted in the ocean model of Large et al. (1994).

(v) Vertical profiles of velocity demonstrated how the nose of the first front reaches a site and then, as it passes by, momentum is transferred upward by engulfing air from aloft. The height of the current changes with time, from about 10 m following the evening transition to several tens of m towards late evening. The vertical momentum diffusion time could be estimated using the model of Brazel et al. (2005).

(vi) Signatures of $PM_{10}$ (coarse dust) entrainment were evident during the arrival of the first transition front, but the entrained amount was dependent on local land use. Thus, significantly higher $PM_{10}$ levels were noted at the PHX site compared to the MVHS site. Subsequent frontal and turbulent mixing events contributed to increase $PM_{10}$ concentration, but only when the local gradient Richardson number is low enough to trigger vertical mixing. Stable stratification may prevent the penetration of turbulence generated aloft (due to instabilities) to the ground level.

Although TRANSFLEX was designed with the expectation of capturing a dominant evening transition front emanating from eastern mountain ranges, smaller mountains to the south were found to play a crucial role. This may be considered a general observation valid in other areas. Once the katabatic flow is established, it maintains the general direction with incessant disturbances from newly arriving intrusions and internal wave oscillations. The location of initial front formation was not captured in the present study, but in future studies it could be tracked by installing a series of sensors along the slope (e.g., Papadopoulos and Helmis 1999) or using vertical lidar scans. To avoid the effects of nearby mountains on the overall progression of transition fronts, as was observed in the present study, it is advisable to conduct kindred field experiments on isolated slopes or on slopes removed from topographic interference. This allows fundamental investigations on independent transition fronts, without contamination of cross flows. A series of towers and/or lidar would help capture in time the frontal processes, flow reversal and turbulence along the current. Such experiments could provide further information on mechanisms causing the evening transitions, especially the conditions for the occurrence of different transition scenarios.

**Acknowledgments** The authors wish to thank Randy Redman and Peter Hyde (Arizona Department of Environmental Quality), Jennifer McCulley, Adam Christman, Dragan Zajic, Charles Retallack, Martin Weeden, Richard Montenegro and Anna Haywood (Arizona State University), Steve Shackleford (Federal Aviation Administration), Mark Sandomir (Mountain View High School), and the Maricopa County Air Quality

Department team without whom TRANFLEX would not have been possible. In addition, the authors thank Niyati Parikh Yagnik for her work on the pattern recognition algorithm. The authors also wish to acknowledge the three anonymous reviewers of this manuscript for making very valuable comments. The financial support for the experiments was provided by the National Science Foundation (NSF-ATM) and Arizona Department of Environmental Quality. The data analysis was performed with the support of NSF (CMG) and the Mountain Terrain Atmospheric Modeling and Observations (MATERHORN) Program, which is supported by the Office of Naval Research.

## References

Arimoto R, Webb JL, Conely M (2005) Radioactive contamination of atmospheric dust over southeastern New Mexico. Atmos Environ 39:4745–4754

Brazel AJ, Fernando HJS, Hunt JCR, Selover N, Hedquist BC, Pardyjak ER (2005) Evening transition observations in Phoenix, Arizona. J Appl Meteorol 44:99–112

Caughey SJ, Kaimal JC (1977) Vertical heat flux in the convective boundary layer. Q J R Meteorol Soc 103:811–815

Chan WC (2001) The modeling of anabatic flow in complex terrain. MS Thesis, Arizona State University

Chen F, Dudhia J (2001) Coupling an advanced land-surface/hydrology model with the Penn State/NCAR MM5 modeling system. Part II: Preliminary model validation. Mon Weather Rev 129:587–604

Choi YJ, Hyde P, Fernando HJS (2006) Modeling of episodic particular matter events using a 3-D air quality model with fine grid: applications to a pair of cities in the U.S./Mexico border. Atmos Environ 40:5181–5201

Cole G, Fernando HJS (1998) Decay of turbulent fluctuations in a convecting boundary layer. Fluid Dyn Res 23(3):161–176

De Silva IPD, Fernando HJS (1998) Experiments on collapsing turbulent regions in stratified fluids. J Fluid Mech 358:29–60

Doran JC, Fast JD, Horel J (2002) The VTMX 2000 campaign. Bull Am Meteorol Soc 83:537–551

Dudhia J (1989) Numerical study of convection observed during the winter monsoon experiment using a mesoscale two-dimensional model. J Atmos Sci 46:3077–3107

Dupont S, Otte TL, Ching JKS (2004) Simulation of meteorological fields within and above urban and rural canopies with a mesoscale model (MM5). Boundary-Layer Meteorol 113:111–158

Fernando HJS (2010) Fluid dynamics of urban atmospheres in complex terrain. Annu Rev Fluid Mech 42:365–389

Fernando HJS, Weil J (2010) Whither the stable boundary layer? A shift in the research agenda. Bull Am Meteorol Soc 91:1475–1484

Fernando HJS, Lee SM, Anderson J, Princevac M, Pardyjak ER, Grossman-Clarke S (2001) Urban fluid mechanics: air circulation and contaminant dispersion in cities. Environ Fluid Mech 1:107–164

Fernando HJS, Zajic D, Di Sabatino S, Dimitrova R, Hedquist B, Dallman A (2010) Flow, turbulence and pollutant dispersion in urban atmospheres. Phys Fluids 22:051301–051319

Hunt JCR, Fernando HJS, Princevac M (2003) Unsteady thermally driven flows on gentle slopes. J Atmos Sci 60:2169–2182

Large WG, McWilliams JC, Doney SC (1994) Oceanic vertical mixing: a review and a model with a vertical K-profile boundary layer parameterization. Rev Geophys 32:363–403

Lee SM, Fernando HJS, Princevac M, Zajic D, Sinesi M, McCulley J, Anderson J (2003) Transport and diffusion of ozone in the nocturnal and morning PBL of the Phoenix Valley. J Environ Fluid Mech 3:331–362

Lee SM, Fernando HJS, Grossman-Clarke S (2007) MM5–CMAQ–SMOKE as a modeling tool for 8-hour ozone regulatory enforcement: applications to the State of Arizona. Environ Model Predict 12:63–74

Monti P, Fernando HJS, Princevac M, Chan WC, Kowalewski TA, Pardyjak ER (2002) Observations of flow and turbulence in the nocturnal boundary layer over a slope. J Atmos Sci 59:2513–2534

Nadeau DF, Pardyjak ER, Higgins CW, Huwald H, Parlange MB (2012) Flow during the evening transition over steep Alpine slopes. Q J R Meteorol Soc, online first 3 July. doi:10.1002/qj.1985

Papadopoulos KH, Helmis CG (1999) Evening and morning transition of katabatic flows. Boundary-Layer Meteorol 92:195–227

Pardyjak ER, Monti P, Fernando HJS (2002) Flux Richardson number measurements in stable atmospheric shear flows. J Fluid Mech 449:307–316

Pardyjak ER, Fernando HJS, Hunt JCR, Grachev AA, Anderson J (2009) A case study of the development of nocturnal slope flows in a wide open valley and associated air quality implications. Meteorol Zeit 18:1–17

Park KS, Fernando HJS (2006) The use of an urban canopy parameterization for MM-5: application to the Phoenix airshed. Paper n. 4.14, 6th symposium on urban environments, 86th AMS annual meeting of the American Meteorological Society, Atlanta, GA, Jan 29–Feb 2

Princevac M (2003) Dynamics of thermal circulation in complex terrain. PhD Dissertation, Arizona State University

Princevac M, Fernando HJS (2007) A criterion for the generation of turbulent anabatic flows. Phys Fluids 19:05102

Princevac M, Fernando HJS (2008) Morning breakup of cold pools in complex terrain. J Fluid Mech 616:99–109

Princevac M, Hunt JCR, Fernando HJS (2008) Quasi-steady katabatic winds over long slopes in wide valleys. J Atmos Sci 65:627–643

Schumann U (1990) Large-eddy simulation of the upslope boundary layer. Q J R Meteorol Soc 116:637–670

Seinfeld JH, Pandis SN (1998) Atmospheric chemistry and physics: from air pollution to climate change. Wiley, New York, 1326 pp

Shafran PC, Seaman NL, Gayno GA (2000) Evaluation of numerical predictions of boundary layer structure during the Lake Michigan ozone study. J Appl Meteorol 39:412–426

Strang EJ, Fernando HJS (2001) Entrainment and mixing in stratified shear flows. J Fluid Mech 428:349–386

Turner JS (1973) Buoyancy effects in fluids. Cambridge University Press, Cambridge, UK, 367 pp

US EPA, US Environmental Protection Agency, Office of Air Quality Planning and Standards (1996) Review of national ambient air quality standards for particulate matter: policy assessment of scientific and technical information. US EPA, Washington, DC, Report No. EPA-452/R-96-013, 305 pp

Verhoef BD (2006) Evening transition in complex terrain: the Phoenix transition flow experiment (TRANSFLEX). MSc Thesis, Arizona State University

Whiteman CD (1982) Breakup of temperature inversions in deep mountain valleys: part I. Observations. J Appl Meteorol 21:270–289

Whiteman CD (1990) Observations of thermally developed wind systems in mountainous terrain. Chapter 2 in W Blumen (ed) Atmospheric processes over complex terrain. Meteorological monographs 23 (no. 45), American Meteorological Society, Boston, MA, pp 5–42

Whiteman CD (2000) Mountain meteorology: fundamentals and applications. Oxford University Press, Oxford, 355 pp

Whiteman CD, McKee TB (1982) Breakup of temperature inversions in deep mountain valleys: part II. Thermodynamic model. J Appl Meteorol 21:290–302

Yagnik N, Liu H, Fernando HJS (2011) Sensor networks: decentralized monitoring and subspace classification of events. Int J Gen Syst 40(4):457–483

Zardi D, Whiteman CD (2012) Diurnal mountain wind systems. Chapter 2 in Chow FK, DeWekker SFJ, Snyder B (eds) Mountain weather research and forecasting. Springer, Berlin, pp 35–119